Journal Pre-proof

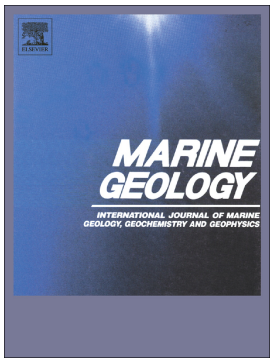

Numerical analysis of the dynamic gas hydrate system and multiple BSRs in the Danube paleo-delta, Black Sea

Shubhangi Gupta, Christian Deusner, Ewa Burwicz-Galerne, Matthias Haeckel

PII: S0025-3227(24)00005-7

DOI: https://doi.org/10.1016/j.margeo.2024.107221

Reference: MARGO 107221

To appear in: *Marine Geology*

Received date: 23 October 2023

Revised date: 15 January 2024

Accepted date: 19 January 2024

Please cite this article as: S. Gupta, C. Deusner, E. Burwicz-Galerne, et al., Numerical analysis of the dynamic gas hydrate system and multiple BSRs in the Danube paleo-delta, Black Sea, *Marine Geology* (2023), https://doi.org/10.1016/j.margeo.2024.107221

Numerical analysis of the dynamic gas hydrate system and multiple BSRs in the Danube paleo-delta, Black Sea

Shubhangi Gupta[a,b], Christian Deusner[b], Ewa Burwicz-Galerne[c], Matthias Haeckel[b]

[a] *Department of Geosciences, University of Malta, Msida, Malta*

[b] *GEOMAR Helmholtz Center for Ocean Research, Kiel, Germany*

[c] *MARUM - Center for Marine Environmental Sciences, University of Bremen, Bremen, Germany*

Abstract

The gas hydrate stability zone (GHSZ) is defined by pressure-temperature-salinity (pTS) constraints of natural gas hydrate (GH) system. It refers to a depth interval which usually extends several hundred meters into the sediment column at sufficient water depths. The lower boundary of the GHSZ often coincides in seismic reflection data with a bottom simulating reflector (BSR), which indicates the transition between the underlying free gas and the overlying no-free gas zone at the thermodynamic stability boundary. The GHSZ in geological systems is dynamic and can shift in response to sedimentation processes and/or changes in environmental conditions such as bottom water temperatures, hydrostatic pressure, and water salinity. The appearance of multiple BSRs has been interpreted as remnants of former GHSZ shifts which have persisted over geological timescales. In this study, we numerically simulate the sedimentation-driven development of multiple stacked BSRs in the Danube deep-sea fan in the Black Sea. We show that in this dynamic sediment depositional regime sufficient amounts of residual gas remain trapped in the former GHSZ, given sufficiently high initial gas hydrate saturations, so that paleo-BSRs could persist over long time scales (~ 300 kyr). In particular, the formation and persistence of multiple BSRs in the Danube Delta is controlled by the sequence of sedimentation events of the levees induced by sea-level change. The kinetics of methane phase transitions between gas hydrate, dissolved methane, and free gas plays a key role in the coexistence, location and timing of the multiple BSRs. Thus, For a given permeability, distinct multiple BSRs appear only for a narrow range of GH formation ($10^{-14} < k_f \left[mol / m^2\ Pa\ s \right] \leq 10^{-12}$) and dissociation rates ($10^{-16} < k_d \left[mol / m^2\ Pa\ s \right] < 10^{-14}$).

Keywords: Natural gas hydrates sedimentation-driven dynamics multiple BSRs Danube delta Black Sea numerical study

1. Introduction

A bottom-simulating reflector (BSR) is typically used as a first indication for free gas and, indirectly, gas hydrate accumulations in the subsurface. It is caused by the seismic impedance contrast of high acoustic velocity in water-saturated sediments containing gas hydrates and the low acoustic velocity in gas-bearing sediments below [1]. If the gas hydrate (GH) system is in steady state with the geological and pressure-temperature-salinity (pTS) conditions, the BSR represents the lower boundary of the gas hydrate stability zone (GHSZ) in the sediments and runs parallel to the seafloor topography. Based on these assumptions, the depth of the BSR is often used to infer the local geothermal gradient (e.g. [2]) or the potential amount of gas hydrates in marine sediments (e.g. [3]).

However, the positioning of the GHSZ is dynamic and sensitive to changes in the local and regional pTS state, and it can shift in response to changes at its upper and lower boundary. For instance, the GHSZ can shrink in response to higher bottom water temperatures, lowering of hydrostatic pressure during sea level drops or increasing seawater salinity, or it can shift upwards due to the deposition of sediment layers and associated re-adjustment of the geothermal profile. An upward shift or shrinking of the GHSZ leads to decomposition of the gas hydrate, either at the top or the bottom of the former GHSZ. At high sediment permeability the released gas can freely migrate upwards through the pore network, whereas in low-permeability, fine-grained sediments it accumulates in place until the pore pressure has increased so much that the sediment fractures, typically forming local migration pathways, such as pipe and chimney structures (e.g. [4]). When entering the new GHSZ, the gas will be immobilized as gas hydrate again, while under high-velocity migration conditions some of the gas may pass through the GHSZ and escape into

the overlying water column (e.g. [5]). In fact, the gas hydrate layer in the path of the upward migrating gas behaves like a converging-diverging mechanical nozzle with decelerating-accelerating fluid flow through the GHSZ, which leads to highly dynamic and cyclic rebuilding of GH at the base of a continuously evolving GHSZ [6, 7].

Considering the time scales of sediment accumulation and burial at most geological locations, it is reasonable to assume steady state conditions, where gas hydrate dissociation and upward gas migration into the new GHSZ drive a smooth shifting of a single BSR such that the BSR remains at the same position relative to the seafloor. However, the presence of two or more distinct BSRs located a few tens of meters above each other has been reported from multiple sites [8, 9, 10, 11, 12]. Several explanations for the occurrence of multiple BSRs have been proposed, including the presence of different gas compositions [9, 10, 13, 14] or anomalously high pressure conditions below the depth of the theoretical BSR [15]. Other studies suggest that multiple BSRs represent former positions of the lower boundary of the GHSZ [8, 16, 9, 17, 18], implying that free gas, and possibly also gas hydrate, has been preserved at the depth of these paleo-BSRs below the modern GHSZ. In agreement with this hypothesis, multiple BSRs have been related to shifts of the GHSZ caused by dynamic changes of pTS conditions during glacialâ€“interglacial transitions or glacial sedimentation events [19, 20].

Similarly, [17] showed that a stack of four well-defined BSRs in the western part of the paleo Danube delta is related to the accumulation of thick levee deposits during glacial sea level low-stands. While the sea level drops below the height of the Bosphorus sill (at 40 m below today's sea level) the Black Sea is disconnected from the inflow of Mediterranean seawater and essentially becomes a freshwater lake. Saline conditions re-establish during interglacial periods, when the sea level rises again. Four limnic phases, i.e. transitions from a marine to a limnic and

back to a marine stage, have been documented to have occurred over the past 300 ka in the Black Sea [21]: sediment sulphur contents are elevated during marine stages as a result of organoclastic sulphate reduction, but are low during limnic stages. Based on global sea level reconstruction data, [22] assigned ages to levee deposits identified in seismic data of the paleo Danube delta, and [17] correlated the top of those deposits, which represent the location of paleo seafloors, to the multiple BSRs as indicators of corresponding base of the paleo GHSZs.

In this study, we analyse under which conditions the free gas released from dissociating gas hydrates can prevail for up to 300 ka and the transport-reaction dynamics that control the formation of the multiple BSRs in the western paleo Danube delta. We have developed a 2D multiphase transport-reaction model to constrain the rates of gas hydrate dissociation and crystallization, gas phase migration, methane dissolution and diffusion as well as gas hydrate saturation and thickness, the permeability of the deposited levee sediments. The model is forced by the geological history of levee deposition and the glacial-interglacial changes of bottom water pTS conditions over the past 300 ka.

2. Geological setting

The lithostratigraphy in the paleo Danube delta of the Black Sea is controlled by dynamic sediment input from the Danube and the Dniepr rivers, as well as by alternating marine and limnic periods that are driven by glacial-interglacial cycles affecting the sea level and bottom water temperatures and salinities of the Black Sea [21]. During the past 500 ka, the Black Sea has experienced five marine stages that were interrupted by four limnic stages, i.e. glacial periods when the sea level dropped below the height of the Bosphorus sill (today at 40 m water depth), thereby, disconnecting the Black Sea from saltwater inflow from the Marmara and Mediterranean Sea and

thus turning the Black Sea into a freshwater lake [22]. A drop of the sea level by $100-150$ m also shifted the river mouths towards today's shelf break resulting in in the development of stacked channel-levee systems on the slopes and extended deep sea fans (Figure 1). West of the Viteaz canyon and its main paleo Danube channel, which has been active during the last glacial period about 25 ka BP [22], a stack of four BSRs has been identified in seismic data (Fig. 1c), each characterized by high amplitude reflection having reversed phase polarity with respect to the seafloor reflector. The shallowest BSR 1 occurs at about $320-380$ m below the seafloor (mbsf) and indicates the base of the present GHSZ. It can be identified in seismic data throughout most parts of the Danube deep-sea fan [23, 24, 9]. The underlying three BSRs (numbered 2-4) are observed, with few exceptions, below and within the well-stratified western levee deposits of a buried channel-levee complex (BCL), but not underneath its channel axis [17]. The BCL likely developed during limnic stages of the Black Sea between 500 and 320 ka BP, i.e. in the time between marine isotope stages (MIS) 13 and 9 [21, 22]. Between 320 and 75 ka BP, the BCL was buried under a relatively even and well-stratified sediment cover (layer A in Fig. 1c), which largely preserved the seafloor topographical characteristics. Over the past 75 ka during the last major glacial period, the main paleo Danube channel has buried the BCL and layer A by thick levee deposits with increasing thickness from SW to NE direction, which has overprinted past topographical features (Fig. 1c).

While the limnic-marine transition in the Black Sea from the last glacial maximum (LGM) to the present has been reconstructed quite robustly, only little is known about the conditions of previous glacial and interglacial periods. Hence, we can only use the present and the LGM conditions as suitable analogies. Today's marine bottom water temperature and salinity are basin-wide very homogeneously at $\sim 9^{\circ}$ C and ~ 22, respectively (e.g., [2]. For the limnic

situation at the last LGM [25] derived a bottom water temperature of 4° C and a salinity of 1, and estimated that reconnection of the Black Sea to the Marmara and Mediterranean Seas occurred about 9 ka before present (BP) [26], and stable marine conditions were established only about 2 ka BP [25]. The downward progressing diffusion front of salt concentrations has reached $20-25$ m into the sediments of the paleo Danube delta [27, 25] and salinities remain relatively constant at $1-3$ further below until 143 mbsf [2]. As a consequence, the GHSZ for methane hydrates in the deeper sediment strata starts at water depths of 665 m, whereas at the seafloor water depths of >720 m are needed [17]. The geothermal gradient in Black Sea sediments is rather poorly constrained, because heat flow measurement in the surface sediments are strongly affected by erosion and deposition from local sediment slumping events and local topography of incised channels [28]. Zander et al. [17] estimated a regional geothermal gradient of $35\pm5^{\circ}$ C/km in the western paleo Danube delta based on the paleo GHSZs indicated by the multiple BSRs. This value agrees quite well with the measured temperature gradient at the DSDP Site 379A [29]. The gas sampled at active vent sites, gas hydrates and dissolved in the porewater of the paleo Danube delta is composed of biogenic methane with only traces of higher hydrocarbons [30, 27].

3. Computational model

3.1. Model equations

We used a multiphase reactive transport model with an advanced numerical simulator for gas hydrate systems in marine subsurface environments [31]. Our mathematical model accounts for the following physical and geochemical processes, which are essential for simulating the highly dynamic methane hydrate system of the paleo Danube delta of the Black Sea:

a) The advective flow of gas and water is described assuming Darcy's law.

b) Capillary effects at the gas-water interface are modelled applying the Brooks-Corey parameterization [32].

c) Gas hydrate phase changes are modelled as a kinetic reaction driven by the difference between methane partial pressure and the equilibrium pressure with respect to the hydrate phase [33]:

$$g^{CH_4} = k^r M^{CH_4} A_{rs} \left(P_e - P_g \right) \tag{1}$$
$$g^{H_2O} = g^{CH_4} N_h \frac{M^{H_2O}}{M^{CH_4}}$$
$$g^{CH_4} + g^{H_2O} + g^h = 0$$

where g^κ for $\kappa = \{CH_4, H_2O, h\}$ denotes the rate of methane, water and gas hydrate produced by a phase change; P_g is the methane partial pressure in the gas phase; P_e is the methane equilibrium pressure with respect to hydrate phase (eqn. 6); k_r is the kinetic rate constant (GH dissociation: $k_r = k_d$ if $P_g < P_e$, and GH formation: $k_r = k_f$ if $P_g \geq P_e$); A_{rs} is the specific reaction surface area (eqn. 4); M^κ denotes the molar weights of $\kappa = \{CH_4, H_2O, h\}$; and N_h is the hydration number (i.e. number of water molecules per methane molecule in the hydrate phase).

d) Hydraulic property changes due to gas hydrate formation or dissociation are modelled following [34, 31]:

$$P_c = p_0 \, S_{we}^{-1/\lambda} \tag{2}$$

$$K = K_0 \left(1 - S_h\right)^{\frac{5m+4}{2m}} \tag{3}$$

$$A_{rs} = \Gamma_r \left(1 - S_h\right)^{\frac{3}{2}} \tag{4}$$

$$\text{s.t.},\Gamma_r = \begin{cases} S_h & \text{for } \left(P_e - P_g\right) > 0 \\ S_g S_w & \text{for } \left(P_e - P_g\right) \le 0 \end{cases},$$

where, P_c is the capillary pressure, p_0 is the gas phase entry pressure, $S_{we} = \frac{S_w - \left(S_{wr} + S_{gr}\right)}{1 - S_h - \left(S_{wr} + S_{gr}\right)}$ is the normalized water phase saturation with irreducible saturations S_{wr} and S_{gr}, respectively; the soil specific parameter λ is a measure of pore size distribution, S_w and S_h are the water and hydrate phase saturations, respectively, K is the absolute permeability of the hydrate bearing sediment, K_0 is the absolute permeability of the corresponding hydrate-free sediment; the soil specific parameter $0 < m \le 3$ describes the sphericity of the soil grains with $m = 3$ for perfectly spherical grains, A_{rs} is the available reaction surface area in the pore spaces of the hydrate-bearing sediment.

e) Porewater salinity is considered by explicitly modelling the transport of dissolved salt mole-fractions, since they affect the local equilibrium state of the hydrate phase.

f) Gas-water miscibility is modelled assuming vapour-liquid-equilibrium (VLE) and considering the appearance and disappearance of respective phases.

g) Thermal effects that arise due to the non-isothermal nature of hydrate phase changes and the strong temperature dependence of hydrate-gas-water phase equilibria, are parameterized by:

$$Q_h = \frac{g_h}{M_h}\left(a_1 + a_2 T\right) \tag{5}$$

$$P_e = 10^6 \exp\left(\begin{array}{l} b_1 + b_2 T + \frac{b_3}{T} + b_4 \ln T \\ + b_5 S\left(b_6 + b_7 T - b_8 T^2 + \frac{b_9}{T} + b_{10} \ln T\right) \\ + b_{11} S^2\left(b_{12} + b_{13} T + b_{14} T^2 - \frac{b_{15}}{T} - b_{16} \ln T\right) \end{array}\right) \quad (6)$$

where Q_h is the volumetric heat generation rate as a result of the kinetic phase change, with parameters $(a_1 = 56599, a_2 = -16.744)$, and P_e is the gas pressure in equilibrium with a gas hydrate phase, parameterized after [35] ($b_1 = -1.6892692 \times 10^3$, $b_2 = -0.15162984$, $b_3 = 5.60912482 \times 10^4$, $b_4 = 2.72067506 \times 10^2$, $b_5 = 5.5354128 \times 10^2$, $b_6 = 2.06621298 \times 10^4$, $b_7 = 14.18127$, $b_8 = 8.3417066 \times 10^{-3}$, $b_9 = -3.78757519 \times 10^5$, $b_{10} = -4.01544417 \times 10^3$, $b_{11} = 3.06407949 \times 10^5$, $b_{12} = 6.04018045 \times 10^2$, $b_{13} = 0.420253434$, $b_{14} = -2.501548 \times 10^{-4}$, $b_{15} = -1.09745335 \times 10^4$, and $b_{16} = -1.17640966 \times 10^2$). T and S are the absolute temperature and salinity, respectively.

h) The dependence of the phase properties (e.g., densities, viscosities, methane solubility, thermal properties, and diffusion coeï¬cients) on pressure, temperature and salinity is parameterized according to the SUGAR-Toolbox [36].

3.2. Model domain

The initial computational domain (Fig. 2) covers the extent of the BCL on the regional seismic line (Fig. 2c): it is 20 km wide and at minimum 800 m high. At the upper surface the model domain follows the paleo seafloor at 300 ka BP (i.e. PSF-C). The base of the gas hydrate stability zone

(bGHSZ) is calculated about 400 m below PSF-C based on the initial pTS conditions prescribed in the domain: temperature at PSF-C is $T_b = 4^\circ$C; within the domain a regional thermal gradient of 35° C/km is set, pressure at PSF-C is 15 MPa, corresponding to a water depth of $\sim$1500 m; within the domain, a hydrostatic pressure distribution is assumed; a constant salinity of 3 is assumed in the model domain. In this study, we ignore changes in sea level and salinity during the glacial-interglacial cycles, and only focus on the effects of sediment accumulation. We further assume that no free gas is present in the domain at $t = 300$ ka BP (i.e., at the start of the simulation). However, the porewater is assumed to be saturated with dissolved methane. Initial permeability is assumed to be 1 mD representing silty clay, and the initial porosity is 0.5, a representative value observed in the eastern part of the paleo Danube delta in sediment depths of $40-140$ mbsf [37]. The GH layer is assumed to sit just above the base of the GHSZ. We consider a quadratic distribution of GH along the depth within the initial GH layer:

$$\left.\frac{S_h}{S_h^*}\right|_{t_0} = 4 \cdot \frac{z}{h}\left(1-\frac{z}{h}\right) \tag{7}$$

where, S_h^* denotes the maximum hydrate saturation, h denotes the initial thickness of the hydrate layer, and $0 \geq z \geq h$ is any point along the Z-axis lying within the hydrate layer at $t_0 = 300$ ka BP. The corresponding hydrate volume is given by:

$$V_{h,0} = \frac{2}{3} \cdot h \cdot S_h^* \tag{8}$$

Three sedimentation events, representing the three glacial limnic phases in the past 300 ka, are modelled, interrupted by periods of no sedimentation, representing the interglacial marine stages: (Event-1) $300 \leq t[\text{ka BP}] \leq 240$, (Event-2) $193 \leq t[\text{ka BP}] \leq 137$, and (Event-3) $75 \leq t[\text{ka BP}] \leq 0$ (see Fig. 2). The sedimentation rate of each sedimentation event is approximated as the total

thickness of the deposited layer over the total duration of that sedimentation event. We assume that the actual surface of the seafloor at any time $t > 300$ ka BP remains in equilibrium with the bottom water conditions. Therefore, the temperature and pressure at the PSF-C evolve over time following the propagation of the thermal and the hydrostatic gradients.

3.3. Numerical scheme

The mathematical model is strongly coupled and highly nonlinear. The governing equations are discretized in space using a fully-upwinded, locally mass-conservative, cell-centered finite volume scheme, and in time using an implicit Euler scheme. The fluxes are approximated using an orthogonal two-point stencil. The discrete model is linearized using a semi-smooth Newton method, which can handle the phase transitions more robustly and is computationally cheaper than a standard Newton solver with primary variable switching. The resulting linear system is solved using a parallel algebraic multigrid (AMG) solver with a stabilized bi-conjugate gradient method as a preconditioner and a symmetric successive over-relaxation smoothening algorithm (part of the built-in DUNE-ISTL library [38]). The numerical scheme is implemented within the DUNE-PDElab framework [39, 31]. The numerical simulator is versatile in terms of the geometry of the computational domain, dimensionality of the problem (2D, 3D), and the implementation of the boundary conditions. The numerical simulations for this study were executed on a NEC HPC-Linux-Cluster, which is part of the hybrid NEC high performance system at the Computing Centre of the Christian Albrechts University in Kiel, Germany.

4. Results

The simulation study was carried out to investigate the dynamic response of free gas and GH accumulations to shifting GHSZ conditions induced by sediment deposition events of the paleo Danube river channel-levee systems in the course of glacial-interglacial sea level changes (Fig. 2), and in particular to constrain the conditions under which the observed multiple BSRs have been formed and preserved over the past 300 ka. The simulation is started at $t = 300$ ka BP assuming that the initial paleo-seafloor corresponds to the seismic reflector PSF-C (Fig. 1,2). The location of the corresponding paleo-BSR is calculated 400 m below this paleo-seafloor (green and back lines in Fig. 2, respectively), thus matching the observed BSR 4 (Fig. 1). Numerical simulations were run for various initial amounts of GH ($V_{h,0}\left[m^3/m^2\right] = \{0.6, 1.8, 6, 10, 15\}$; Tab. 1). An intrinsic permeability (K_0) of 10^{-15} m^2 was assigned throughout the sediment domain to impose low intrinsic flow restrictions. Local permeability was reduced by GH as defined in Eqn. 3.

It was shown in [6] that the dynamics of gas migration through the GHSZ is essentially a balance of the upward buoyancy force, the downward burial force, and the flow modulation (i.e. acceleration/deceleration) by the GH layer that forms in the path of the migrating free gas. In that sense, the GH layer acts like a 'mechanical' nozzle, the shape of which is continuously evolving based on the rate of hydrate phase change, and in turn, resulting in a very rich internal dynamics which the authors refer as the 'hydrate-nozzle effect'. It was shown that under certain combinations of permeability, burial-rate (constant), and kinetic rate parameters, the GH dynamics can lead to the coexistence of two distinct GH layers, one at the base of the present GHSZ, and one below, corresponding to some previous configuration of the GHSZ. Besides GH inventories and distributions,Therefore, to study the formation of multiple BSRs driven by episodic sedimentation events (i.e., a sequence of burial-rates) we additionally tested different combinations of intrinsic rate constants of GH dissociation (k_d) and formation (k_f).

Other model parameters were specified as outlined in [31]. In particular, the sediment specific parameters (Eqn. 1-4) were chosen as: $p_0 = 5$ kPa, $\lambda = 1.2$ and $m = 0.225$ (for pore-filling GH). The simulations did not take into account any net CH_4 formation through methanogenesis in-situ or migration of CH_4 from deeper sources into the model domain, i.e. the formation of BSRs is entirely based on the internal CH_4 cycling in the domain.

Table 1: Summary of parameters varied in the numerical simulation scenarios. $V_{h,0}$ = initial amount of GH (Eqn. 8), k_d = kinetic constant of GH dissociation, k_f = kinetic constant of GH formation. Scenario Id. 2 is referred to as "best match" scenario since it reproduces the observed multiple BSRs closest (Fig. 3).

Scenario Id.	parameters		
	$V_{h,0} / \frac{m^3}{m^2}$	$k_d / \frac{mol}{m^2 \cdot Pa \cdot s}$	$k_f / \frac{mol}{m^2 \cdot Pa \cdot s}$
1	15	10^{-15}	10^{-13}
2	10	10^{-15}	10^{-13}
3	6	10^{-15}	10^{-13}
4	1.8	10^{-15}	10^{-13}
5	0.6	10^{-15}	10^{-13}
6	10	10^{-15}	10^{-12}
7	10	10^{-15}	10^{-14}
8	10	10^{-14}	10^{-13}
9	10	10^{-16}	10^{-13}

Our simulations match seismic observations best for an initial GH volume of $V_{h,0} = 10$ m^3 /m^2 and applying intrinsic rate constants of GH dissociation of $k_d = 10^{-15}$ mol/(m^2 Pa s) and GH formation of $k_f = 10^{-13}$ mol/(m^2 Pa s) (Fig. 3, scenario 2 in Tab. 1). After 300 ka, the free gas released from the buried and dissociating GH has accumulated in 4 distinct zones below the western and eastern levee deposits (Fig. 3). The simulations also predict multiple distinct gas accumulations below the channel axis, which cannot be resolved in the seismic data due to its noisy, turbid character. The free CH_4 gas zones correlate with distinct GH layers that have reformed after each deposition event, except for the upper zone, which is located above and below the corresponding GH layer due to yet incomplete re-formation of GH (Figs. 3 and 4). Gas saturation values (S_g) show a strong correlation with topographic features, i.e. elevations and depressions of the initial paleo-seafloor (PSF-C) and the thickness of the deposited sediment layer, which is higher in the NE direction (Figs. 2 and 3). In accordance with the seismic observations, no free gas is predicted in regions underlying topographic highs (Fig. 3). In the vicinity of these seafloor peaks, highest gas saturations are found, while below the thick eastern levee deposits a thick free gas zone is established extending upwards (Fig. 3).

The simulation results clearly show that each deposition event of levee sediments induces the dissociation of GH and upward migration of released free gas followed by re-formation of a distinct GH layer at the base of a newly established GHSZ, overall resulting in the formation of multiple BSRs (Fig. 3 and 4). Interestingly, the continuous initial GH layer develops into distinct but discontinuous free gas and GH layers (Fig. 4). Similar to distributions of free gas, the discontinuities of the new GH layers appear to be related to seafloor topographic highs. At these locations, GH accumulations remain relatively stable in place over the simulation time of 300 ka

and, as a consequence, only little to no free gas is released here (Fig. 4). In contrast, below the levees and channel axis the initial GH layer has completely disappeared after 300 ka, however traces of free gas remain at this depth.

The initial temperature distribution (Fig. 2B(a)) is strongly altered by GH dynamic phase-changes and convective transport driven by fluid fluxes along the topographic gradients (Fig. 5d-f). Substantial heterogeneities of dissolved CH_4 concentrations evolved during the simulation (Fig. 5g-i), which are especially pronounced below the GHSZ, directly under the peaks of the paleo seafloor. These heterogeneities are driven by the lateral fluxes of pore-water along the topographic gradients, which not only transport the dissolved methane, salts, and heat away from the peaks, but also promote mixing zone below the paleo-channel. Furthermore, GH phase-changes after gas migration produced strong local salinity gradients (Fig. 5j-l). An increase in salt concentration is observed during GH formation, and vice-versa. Parabolic-shaped zones with high salinity contrasts reaching towards the initial seafloor (PSF-C) indicate that salinity effects from GH dynamics coupled with lateral transport along topographic gradients add further heterogeneity to the initially homogeneous salinity distribution in the model domain. Overall, the results suggest that coupled reactive transport processes strongly affect the positioning of free gas and reformation of GH layers.

Further it can be seen that the initial GH volume strongly affects the distinctiveness and continuity of free gas zones formed in the simulations. For an initial GH amount of $V_{h,0} = 10\ \mathrm{m}^3/\mathrm{m}^2$, sharp stacked gas zones result (Fig. 6), while for smaller initial volumes the resulting free gas zones appear less distinct ($V_{h,0} = 6\ \mathrm{m}^3/\mathrm{m}^2$) until they become quite patchy and discontinuous ($V_{h,0} = \{1.8, 0.6\}\ \mathrm{m}^3/\mathrm{m}^2$). This correlates with complete dissociation of the initial as well as re-formed GH layers within the time period of levee deposition (Fig. 6). At higher initial GH

volumes ($V_{h,0} = 15\ \mathrm{m}^3/\mathrm{m}^2$) the gas concentrations in the vicinity of the GH layers remain high and tend to accumulate in extremely high saturations ($S_g > 0.6$) below the peaks of the seafloor topography, which are likely to trigger geo-mechanical instabilities, and therefore, are unphysical for the geological setting of the study area. On the other hand, at lower inventories distinct fronts are not observed and the gas distributions is more diffuse and blurred. The dominant factor of the initial GH volume is seen when further increasing the value ($V_{h,0} = 15\ \mathrm{m}^3/\mathrm{m}^2$, Fig. 6). Under these conditions, high concentrations of free gas can accumulate below the initial GH layer, and again, this layering is least affected and shifted below initial seafloor elevations, which would make it more likely that seismic analysis identifies distinct BSR signals from paleo-BSRs even at these locations.

A profound effect was observed from varying the intrinsic rate constants for GH dissociation (k_d) and formation (k_f). Decreasing k_d by one order of magnitude (i.e. to 10^{-16} mol/(m^2 Pa s)) seems to affect the initial GH layer only little, whereas an increase by one order of magnitude (i.e. to 10^{-14} mol/(m^2 Pa s)) leads to the complete disappearance of the initial GH layer (Fig. 7). Both of these manifest as continuous free gas zones: the former bounded from below as there is little to no resistance for upward gas migration, while the latter bounded from above as the GH layer closely follows the evolving base of the GHSZ and restricts further upward gas migration. At $k_d = 10^{-15}$ mol/(m^2 Pa s) (best match value), multiple GH layers coexist at the base of GHSZs of each paleo seafloor (Fig. 7), and each of these layers preserves traces of free gas below (Fig. 8) that persist over 300 ka. An increase in k_f by one order of magnitude (i.e. to 10^{-12} mol/(m^2 Pa s)) leads to very sharp GH layers with high saturation (Fig. 7). Corresponding low permeabilities effectively cut off further gas flow through overlying GHSZ, leading to

accumulation of very large amounts of free gas at the base of the actual GHSZ (Fig. 8). On the other hand, a decrease of k_f by one order of magnitude (i.e. to 10^{-14} mol/(m^2 Pa s)) results in a nearly continuous deposition of GH layer (Fig. 7) that offers relatively low resistance to upward gas migration, resulting in a diffuse and blurred free gas distribution (Fig. 8).

5. Discussion

Our simulation results confirm that multiple stacked BSRs observed in the levee deposits of a buried channel-levee system in the Danube deep-sea fan are related to former positions of the GHSZ and can be regarded as paleo-BSRs. The formation of these paleo-BSRs was favored by shifting of the GHSZ in response to sediment deposition events. Our results further suggest that the topographical features and the dynamic re-shaping of the seafloor during sediment deposition could facilitate the formation of discontinuous BSRs. The discontinuities, and sometimes patchiness, of GH and free gas layers is in agreement with the sharp but discontinuous paleo-BSRs interpreted from seismic analysis [17].

We suggest that the potential of multiple-BSR formation strongly dependents on the GH inventory (i.e. the amount of methane in the system). Dynamics of gas migration over geological time scales is strongly related to the initial gas hydrate volume, however, it is not directly influenced by the exact gas hydrate distribution within the sediments. It has been shown In multiple modeling scenarios with variable initial gas hydrate saturations (e.g. $S_h = 50\%$ and $h = 30$ m or $S_h = 30\%$ and $h = 50$ m), where the numerical solution converged towards similar gas migration profile. The preservation of GH at the initial BSR is in agreement with seismic analysis where high amplitude reflections are lacking directly above the paleo-BSRs and the

paleo-BSRs in the high-resolution seismic data were remarkably sharp. [17] concluded that the amount of gas that was formed by GH dissociation had to be very small and that free gas still exists in the zone below the previous GHSZs. This is strongly supported by our calculated amounts of the residual gas, which remains less than 4% at the BSRs.

Furthermore, the kinetics of GH $\leftrightarrow$ gas phase transitions have a strong effect on the multiple BSR formation. For the prescribed permeability field, distinct multiple BSRs occurred for a narrow range of GH formation and dissociation rates. Variations by one order of magnitude of individual rate constants (k_d and k_f) directly change the gas distribution. Specifically, the combination of slow dissociation ($k_d = 10^{-16}$ mol/m^2 Pa s) and fast formation ($k_f = 10^{-12}$ mol/m^2 Pa s) led to the hold-up of substantially larger amounts of gas at greater depths. Our results analyse a specific case-study on globally unique long-lasting preservation of multiple (at least triple) BSRs in marine sediments. It is in agreement with previous work of [17] who suggested that rapid changes in sedimentation regime create favorable conditions for multiple BSR formation. Broadly, it is based upon the gas hydrate recycling concept stating that massive gas hydrate layers with high GH saturations buried below the local GHSZ dissociate and form sufficient amounts of mobile free gas which re-enters newly-established GHSZ and turns into gas hydrate [40, 41]. Our findings stay in agreement with the observations of [6] where rapid sediment burial causes cyclic rebuilding of gas hydrates in a 'limited-gas-supply' setting (i.e. no additional gas sources), similar to this study. System behavior described in [6] shows multiple similarities to our observations from the Danube delta. It basically states that under similar conditions gas hydrate dynamics can exhibit a cyclic nature where a new gas hydrate layer forms at the base of the shifted GHSZ while the old gas hydrate layer, related to some former configuration of the GHSZ, can still persist for over 300 ka in Danube delta despite the unstable pTS thermodynamic conditions. Furthermore, [7]

demonstrated the existence of bifurcation manifolds in the high-dimensional parameter space of the burial-driven gas hydrate dynamics, where these cyclic states appeared only under a narrow combination of burial rates (controlling the downward burial of free-gas), permeability (controlling the up-ward advection of free-gas), and GH kinetic rates (modulating the acceleration-deceleration of gas flow). These results are in agreement with our findings that in the system where sediment permeability and burial rates are known, the kinetic rates of phase transitions remain the most critical factor driving the free gas mobility and ability to accumulate in sedimentary pore space which is the essential condition for the existence of multiple BSRs.

The topographical features of the initially prescribed seafloor and subsequently imposed sediment deposition patterns had a striking effect on the simulation results and showed a distinct correlation with phase distributions below seafloor elevations or depressions, respectively. Temperature shifts and heat transport dynamics favored GH preservation below seafloor elevations, whereas below the paleo channel faster GH dissociation and gas migration was observed, which is in agreement with seismic data. At the NE levee side, which received the highest sediment input, upward gas migration was most pronounced and extended to the former PSF-C. The strong effect of topographical features and sedimentation profiles highlights the necessity to consider 2D or even 3D topographical or structural features in numerical simulations and suggests that 1D simulations may not be sufficient when considering complex terrains, coupled transport processes, and non-equilibrium conditions.

According to our results, multiple-BSRs can evolve and persist after relatively fast shifts of the lower boundary of GHSZ. Thus, a series of rapid mass deposition events at the seafloor are likely important pre-requisites of multi-BSR occurrence. However, other factors, related or unrelated to sediment deposition, such as bottom water temperature or salinity changes may be

supplementing the situation, which was not further considered in this study. The Black Sea in general, and the Danube paleo delta and deep sea fan in particular, have experienced very specific histories of limnic and marine periods with changing water levels and dynamic shifts of sediment input and burial, which favored sediment deposition. This setting is unlike the scenarios at other deltas and estuaries due to the dynamics of the Eurasian ice sheets, which triggered and controlled solids mobilization and transport to the Black Sea. Sea level changes during the Holocene and Pleistocene are primarily a consequence of the cyclic growth and decay of ice sheets [42], which resulted in a complex global and local patterns of solids transport, flooding events, and sea level changes [43, 44, 45, 46, 47, 48]. Fast and irregular shifts of the GHSZ could also occur in response to tectonic uplift, which was suggested to be related to multiple BSR formation [11, 49, 50].

Since it was shown that the formation of multiple BSRs is strongly dependent on GH inventories, we hypothesize that it could also be favored in scenarios of high gas supply, and discontinuous or continuous upward gas migration [51, 52, 12]. Our results show that very high GH saturations require a quite small layer thickness, and high volumes of GH are not necessarily favorable for the formation of multiple BSRs. We did not consider in-situ biogenic CH_4 formation and only focused on a constant CH_4 inventory in each simulation. We hypothesise the in-situ formation of CH_4, even more than upward gas flow into the GHSZ, is expected to favor the formation and preservation of multiple-BSRs during shifts of the GHSZ, because it could act as a CH_4 source in low-permeability sediments with high organic carbon content. Since intense organic matter input and biogenic CH_4 production would be favored at river deltas or estuaries, it is possible that in-situ CH_4 formation has enhanced multiple BSR formation also in the Danube paleo-delta. In fact, [7] (preprint) have shown that in-situ biogenic CH_4 production ensures a

connected gas reservoir below the hydrate-nozzle, and therefore, promotes the nozzle dynamics. The constant gas inventory, used in this study, would be then a limiting case where the gas reservoir below the hydrate nozzle periodically depletes (cutting-off the gas supply to the nozzle throat) and replenishes (re-establishing gas supply to the nozzle throat). In that sense, the limited gas-supply assumption provides a conservative setting to test whether multiple BSRs can be linked to past rapid-sedimentation events.

6. Conclusions

This study provides strong evidence that distinct paleo-BSRs can persist over hundred thousands of years in low-permeability sediments. The primary driver for the formation of multiple BSRs is sedimentation events of several tens of meters, a relatively narrow range of low-permeability sediments and GH kinetic rates (dissociation / reformation). The coexistence of multiple hydrate layers below the GHSZ is explained by the 'hydrate-nozzle' effect, where the relative competition between sediment burial, free-gas buoyancy, and GH kinetics affects the position and continuity of the simulated paleo-BSRs over geological time scales. The key factor for the development of multiple (>2) BSRs is a rapid, episodic and pronounced thermal destabilization of GH at the lower boundary of the GHSZ. As shown in this study, natural sedimentation processes in river deltas and estuaries could, in principal, provide sufficiently high solids input to cause the required shift of the thermal gradient. Thus, the Black Sea geological setting needs to be regarded as a unique system where at least three paleo BSRs have been discovered. This study provides strong evidence that the presence of pronounced topographic features, such as seafloor elevations and depressions, and non-homogeneous sediment deposition favors heterogeneous phase distributions and discontinuities of paleo BSRs, which is in accordance with results from regional seismic

studies.

Funding

This research received joint funding by the German Ministry of Economy and Energy (BMWi) and the German Ministry of Education and Research (BMBF) through the German gas hydrate programme SUGAR (grant nos. 03SX320A, 03G0819A, 03G0856A). SG was supported by the MSCA Postdoctoral ERA Fellowships 2021 action, under the Horizon Europe program, project 'WarmArctic' number 101090338.. EB-G received support from the Cluster of Excellence 'The Ocean Floor – Earth's Uncharted Interface' (EXC 2077) funded by Deutsche Forschungsgemeinschaft (DFG) - Project number 390741603 hosted by the Research Faculty MARUM of the University of Bremen, Germany.

Acknowledgements

SG acknowledges additional support from the SMART Project funded through the Helmholtz European Partnering Initiative (Project ID Number PIE-0004) and the MARCAN Project funded through the European Research Council (Grant No 677898) under European Union's Horizon 2020 research program.

Author Contributions

The authors confirm contribution to the paper as follows: Study conception and design: S.G., M.H.; data collection: S.G., M.H.; model and software development: S.G.; numerical simulations:

S.G., analysis and interpretation of results: S.G, E.B.-G., C.D, M.H; draft manuscript preparation: S.G, C.D, M.H.; figures and movie preparation: S.G.; final manuscript preparation: S.G., E.B.-G, C.D, M.H.

Declarations

The authors have no competing financial interests. No generative AI software was used for scientific writing.

Data and materials availability

The numerical model is implemented within version 2.8 of C++ based DUNE-PDELab framework [39, 38], and uses the in-built matrix assembler, linearization algorithm (Newton method with numerical Jacobian), and linear solver (parallel Algebraic Multi-Grid (AMG) solver with stabilized bi-CG preconditioner). The DUNE libraries used in this study are preserved at https://gitlab.dune-project.org/pdelab/dune-pdelab and developed openly at https://www.dune-project.org/.

The source code for our GH model and the reference test scenario presented in this manuscript is publicly archived and can be accessed as https://doi.org/10.5281/zenodo.8310169.

Supplementary Material

An animation of the numerical solutions for the reference (best-fit) scenario (i.e., the scenario with initial GH inventory $V_{h,0} = 10\,\mathrm{m}^3/\mathrm{m}^2$, and kinetic rates $k_d = 10^{-15}$ and $k_f = 10^{-13}$

$\mathrm{mol}/(m^2 \cdot \mathrm{Pa} \cdot s)$) is included as supplementary information. The public git repository for the code includes the raw numerical solution files for this numerical simulation, which can be visulatized using the freely available ParaView software.

References

[1] R. Hyndman, E. Davis, A mechanism for the formation of methane hydrate and seafloor bottom- simulating reflectors by vertical fluid expulsion, Journal of Geophysical Research 97 (1992) 7025–7041. doi: 10.1029/91JB03061.

[2] M. Riedel, T. Freudenthal, J. Bialas, C. Papenberg, M. Haeckel, M. Bergenthal, T. Pape, G. Bohrmann, In-situ borehole temperature measurements confirm dynamics of the gas hydrate stability zone at the upper danube deep sea fan, black sea, Earth and Planetary Science Letters 563 (2021) 116869. doi: 10.1016/j.epsl.2021.116869.

[3] G. R. Dickens, The potential volume of oceanic methane hydrates with variable external conditions, Organic Geochemistry 32 (2001) 1179–1193. doi: 10.1016/S0146-6380(01)00086-9.

[4] C. Berndt, Focused fluid flow on continental margins, Philosophical transactions. Series A, Mathematical, physical, and engineering sciences 363 (2005) 2855–71. doi: 10.1098/rsta.2005.1666.

[5] J. Liu, M. Haeckel, J. Rutqvist, S. Wang, W. Yan, The mechanism of methane gas migration through the gas hydrate stability zone: Insights from numerical simulations, Journal of Geophysical Research: Solid Earth 124 (2019) 4399–4427. doi: 10.1029/2019JB017417.

[6] C. Schmidt, S. Gupta, L. Rüpke, E. Burwicz-Galerne, E. H. Hartz, Sedimentation-driven

cyclic rebuilding of gas hydrates, Marine and Petroleum Geology 140 (2022) 105628. doi: 10.1016/j.marpetgeo.2022.105628.

[7] S. Gupta, E. Burwicz-Galerne, C. Schmidt, L. Rüpke, Periodic states and their implications in gas hydrate systems, Earth and Planetary Science Letters 624 (2023) 118445. doi: https://doi.org/10.1016/j.epsl.2023.118445.

[8] J.-P. Foucher, H. Nouzé, P. Henry, Observation and tentative interpretation of a double bsr on the nankai slope, Marine Geology 187 (2002) 161–175. doi: 10.1016/S0025-3227(02)00264-5.

[9] I. Popescu, M. De Batist, G. Lericolais, H. Nouzé, J. Poort, N. Panin, W. Versteeg, H. Gillet, Multiple bottom-simulating reflections in the black sea: Potential proxies of past climate conditions, Marine Geology 227 (2006) 163–176. doi: 10.1016/j.margeo.2005.12.006.

[10] R. Geletti, M. Busetti, A double bottom simulating reflector in the western ross sea, antarctica, Journal of Geophysical Research: Solid Earth 116 (2011). doi: 10.1029/2010JB007864.

[11] I. Pecher, H. Villinger, N. Kaul, G. Crutchley, J. Mountjoy, K. Huhn, N. Kukowski, S. Henrys, P. Rose, R. Coffin, A fluid pulse on the hikurangi subduction margin: Evidence from a heat flux transect across the upper limit of gas hydrate stability, Geophysical Research Letters 44 (2017) 12,385–12,395. doi: 10.1002/2017GL076368.

[12] W. Zhang, J. Liang, Z. Wan, P. Su, W. Huang, L. Wang, L. Lin, Dynamic accumulation of gas hydrates associated with the channel-levee system in the shenhu area, northern south china sea, Marine and Petroleum Geology 117 (2020). doi: 10.1016/j.marpetgeo.2020.104354.

[13] M. Paganoni, J. Cartwright, M. Foschi, R. Shipp, P. Van Rensbergen, Structure ii gas hydrates found below the bottom-simulating reflector, Geophysical Research Letters 43 (2016) 5696–5706. doi: 10.1002/2016GL069452.

[14] R. Jatiault, L. Loncke, D. Dhont, P. Imbert, D. Dubucq, Geophysical characterisation of active thermogenic oil seeps in the salt province of the lower congo basin part i: Detailed study of one oil-seeping site, Marine and Petroleum Geology 103 (2019) 753–772. doi: 10.1016/j.marpetgeo.2018.11.026.

[15] U. Tinivella, M. Giustiniani, Variations in bsr depth due to gas hydrate stability versus pore pressure, Global and Planetary Change 100 (2013) 119–128. doi: 10.1016/j.gloplacha.2012.10.012.

[16] G. Netzeband, C. Hübscher, D. Gajewski, J. Grobys, J. Bialas, Seismic velocities from the yaquina forearc basin off peru: Evidence for free gas within the gas hydrate stability zone, International Journal of Earth Sciences 94 (2005) 420–432. doi: 10.1007/s00531-005-0483-2.

[17] T. Zander, M. Haeckel, C. Berndt, W. C. Chi, I. Klaucke, J. Bialas, D. Klaeschen, S. Koch, O. Atgın, On the origin of multiple BSRs in the Danube deep-sea fan, Black Sea, Earth and Planetary Science Letters 462 (2017) 15–25. doi: 10.1016/j.epsl.2017.01.006.

[18] S. Ker, Y. Thomas, V. Riboulot, N. Sultan, C. Bernard, C. Scalabrin, G. Ion, B. Marsset, Anomalously deep bsr related to a transient state of the gas hydrate system in the western black sea, Geochemistry, Geophysics, Geosystems 20 (2019) 442–459. doi: 10.1029/2018GC007861.

[19] N. Bangs, R. Musgrave, A. Tréhu, Upward shifts in the southern hydrate ridge gas hydrate stability zone following postglacial warming, offshore oregon, Journal of Geophysical

Research: Solid Earth 110 (2005) 1–13. doi: 10.1029/2004JB003293.

[20] R. Davies, K. Thatcher, H. Armstrong, J. Yang, S. Hunter, Tracking the relict bases of marine methane hydrates using their intersections with stratigraphic reflections, Geology 40 (2012) 1011–1014. doi: 10.1130/G33297.1.

[21] E. T. Degens, D. A. Ross, The Black Sea: Geology, chemistry, biology, AAPG Mem. (1974). doi: 10.1306/M20377.

[22] C. Winguth, H. Wong, N. Panin, C. Dinu, P. Georgescu, G. Ungureanu, V. Krugliakov, V. Podshuveit, Upper Quaternary water level history and sedimentation in the northwestern Black Sea, Marine Geology 167 (2000) 127–146. doi: 10.1016/S0025-3227(00)00024-4.

[23] N. Baristeas, Seismische Fazies, Tektonik und Gashydratvorkommen im nordwestlichen Schwarzen Meer, Diploma Thesis, Master's thesis, University of Hamburg, 2006.

[24] M. Haeckel, J. Bialas, I. Klaucke, K. Wallmann, G. Bohrmann, K. Schwalenberg, Gas hydrate occurrences in the black sea â€“ new observations from the german sugar project, Fire In The Ice 15 (2015) 6–9.

[25] G. Soulet, G. Delaygue, C. Vallet-Coulomb, M. BÃ¶ttcher, C. Sonzogni, G. Lericolais, E. Bard, Glacial hydrologic conditions in the black sea reconstructed using geochemical pore water profiles, Earth and Planetary Science Letters 296 (2010) 57–66. doi: 10.1016/j.epsl.2010.04.045.

[26] G. Soulet, G. Ménot, G. Lericolais, E. Bard, A revised calendar age for the last reconnection of the black sea to the global ocean, Quaternary Science Reviews 30 (2011) 1019–1026. doi: 10.1016/j.quascirev.2011.03.001.

[27] L. Ruffine, C. Deusner, M. Haeckel, E. Kossel, S. Toucanne, S. Chéron, A. Boissier, M. Schmidt, J.-P. Donval, F. Scholz, V. Guyader, S. Ker, V. Riboulot, Effects of postglacial

seawater intrusion on sediment geochemical characteristics in the romanian sector of the black sea, Marine and Petroleum Geology 123 (2021) 104746. doi: 10.1016/j.marpetgeo.2020.104746.

[28] M. Riedel, J. Bialas, H. Villinger, T. Pape, M. Haeckel, G. Bohrmann, Heat flow measurements at the danube deep-sea fan, western black sea, Geosciences 11 (2021). doi: 10.3390/geosciences11060240.

[29] A. Erickson, R. Von Herzen, Downhole temperature measurements and heat flow data in the black sea dsdp leg 42b, in: D. Ross, P. Supko (Eds.), Scientific Results of the Deep-Sea Drilling Project 42, Part 2, U.S. Government Printing Office, Washington, 1978, pp. 1085–1103.

[30] T. Pape, M. Haeckel, M. Riedel, M. Kölling, M. Schmidt, K. Wallmann, G. Bohrmann, Formation pathways of light hydrocarbons in deep sediments of the danube deep-sea fan, western black sea, Marine and Petroleum Geology 122 (2020) 104627. doi: 10.1016/j.marpetgeo.2020.104627.

[31] S. Gupta, B. Wohlmuth, M. Haeckel, An all-at-once newton strategy for marine methane hydrate reservoir models, Energies 13 (2020) 503. doi: 10.3390/en13020503.

[32] R. H. Brooks, A. T. Corey, Hydraulic Properties of Porous Media, Colorado State University Hydrology Papers, Colorado State University, 1964.

[33] H. C. Kim, P. R. Bishnoi, R. A. Heidemann, S. S. H. Rizvi, Kinetics of methane hydrate decomposition, Chemical Engineering Science 42 (1987) 1645–1653. doi: 10.1016/0009-2509(87)80169-0.

[34] S. Gupta, R. Helmig, B. Wohlmuth, Non-isothermal, multi-phase, multi-component flows through deformable methane hydrate reservoirs, Computational Geosciences 19 (2015)

1063–1088. doi: 10.1007/s10596-015-9520-9.

[35] P. Tishchenko, C. Hensen, K. Wallmann, C. S. Wong, Calculation of the stability and solubility of methane hydrate in seawater, Chemical Geology 219 (2005) 37 – 52. doi: 10.1016/j.chemgeo.2005.02.008.

[36] E. Kossel, N. Bigalke, E. Pinero, M. Haeckel, The SUGAR Toolbox - A Library of Numerical Algorithms and Data for Modelling of Gas Hydrate Systems and Marine Environments, Technical Report Report Nr. 8:160, GEOMAR, Kiel, Germany, 2013.

[37] M. Riedel, T. Freudenthal, M. Bergenthal, M. Haeckel, K. Wallmann, E. Spangenberg, J. Bialas, G. Bohrmann, Physical properties and core-log seismic integration from drilling at the danube deep-sea fan, black sea, Marine and Petroleum Geology 114 (2020) 104192. doi: 10.1016/j.marpetgeo.2019.104192.

[38] O. Sander, DUNE – The Distributed and Unified Numerics Environment, Lecture //notes in Computational Science and Engineering, Springer International Publishing, 2020.

[39] P. Bastian, F. Heimann, S. Marnach, Generic implementation of finite element methods in the Distributed and Unified Numerics Environment (DUNE), Kybernetika 46 (2010) 294–315.

[40] E. Burwicz, T. Reichel, K. Wallmann, W. Rottke, M. Haeckel, C. Hensen, 3-d basin-scale reconstruction of natural gas hydrate system of the green canyon, gulf of mexico, Geochemistry, Geophysics, Geosystems 18 (2017) 1959–1985. doi: 10.1002/2017GC006876.

[41] R. Haacke, G. Westbrook, R. Hyndman, Gas hydrate, fluid flow and free gas: Formation of the bottom-simulating reflector, Earth and Planetary Science Letters 261 (2007) 407–420. doi: 10.1016/j.epsl.2007.07.008.

[42] K. Lambeck, J. Chappell, Sea level change through the last glacial cycle, Science 292 (2001) 679–686. doi: 10.1126/science.1059549.

[43] M. Siddall, E. Rohling, A. Almogi-Labin, C. Hemleben, D. Meischner, I. Schmelzer, D. Smeed, Sea-level fluctuations during the last glacial cycle, Nature 423 (2003) 853–858. doi: 10.1038/nature01690.

[44] J. Svendsen, H. Alexanderson, V. Astakhov, I. Demidov, J. Dowdeswell, S. Funder, V. Gataullin, M. Henriksen, C. Hjort, M. Houmark-Nielsen, H. Hubberten, O. IngÃ³lfsson, M. Jakobsson, K. KjÃ¦r, E. Larsen, H. Lokrantz, J. Lunkka, A. LysÃ¥, J. Mangerud, A. Matiouchkov, A. Murray, P. MÃ¶ller, F. Niessen, O. Nikolskaya, L. Polyak, M. Saarnisto, C. Siegert, M. Siegert, R. Spielhagen, R. Stein, Late quaternary ice sheet history of northern eurasia, Quaternary Science Reviews 23 (2004) 1229–1271. doi: 10.1016/j.quascirev.2003.12.008.

[45] J. Robl, S. Hergarten, K. Stüwe, Morphological analysis of the drainage system in the eastern alps, Tectonophysics 460 (2008) 263–277. doi: 10.1016/j.tecto.2008.08.024.

[46] S. Badertscher, D. Fleitmann, H. Cheng, R. Edwards, O. Göktürk, A. Zumbühl, M. Leuenberger, O. Tüysüz, Pleistocene water intrusions from the mediterranean and caspian seas into the black sea, Nature Geoscience 4 (2011) 236–239. doi: 10.1038/ngeo1106.

[47] A. Wegwerth, O. Dellwig, S. Wulf, B. Plessen, I. Kleinhanns, N. Nowaczyk, L. Jiabo, H. Arz, Major hydrological shifts in the black sea â€œlakeâ€• in response to ice sheet collapses during mis 6 (130–184 ka bp), Quaternary Science Reviews 219 (2019) 126–144. doi: 10.1016/j.quascirev.2019.07.008.

[48] A. Panin, V. Astakhov, E. Lotsari, G. Komatsu, J. Lang, J. Winsemann, Middle and late quaternary glacial lake-outburst floods, drainage diversions and reorganization of fluvial

systems in northwestern eurasia, Earth-Science Reviews 201 (2020). doi: 10.1016/j.earscirev.2019.103069.

[49] A. Antriasian, R. Harris, A. Tréhu, S. Henrys, B. Phrampus, R. Lauer, A. Gorman, I. Pecher, D. Barker, Thermal regime of the northern hikurangi margin, new zealand, Geophysical Journal International 216 (2020) 1177–1190. doi: 10.1093/gji/ggy450.

[50] K. Waghorn, S. Vadakkepuliyambatta, A. Plaza-Faverola, J. Johnson, S. Bünz, M. Waage, Crustal processes sustain arctic abiotic gas hydrate and fluid flow systems, Scientific Reports 10 (2020). doi: 10.1038/s41598-020-67426-3.

[51] M. Paganoni, J. Cartwright, M. Foschi, C. Shipp, P. Van Rensbergen, Relationship between fluid-escape pipes and hydrate distribution in offshore sabah (nw borneo), Marine Geology 395 (2018) 82–103. doi: 10.1016/j.margeo.2017.09.010.

[52] T. Himmler, D. Sahy, T. Martma, G. Bohrmann, A. Plaza-Faverola, S. Bünz, D. Condon, J. Knies, A. Lepland, A 160,000-year-old history of tectonically controlled methane seepage in the arctic, Science Advances 5 (2019). doi: 10.1126/sciadv.aaw1450.

Figure 1: A) Bathymetric map of the western part of the paleo Danube delta. The inset shows the location of the study area in the Black Sea. B) Gray shaded areas depict the outline of the buried channel-levee complex (BCL) and colored lines indicate the extent of BSRs 2-4 as identified on regional seismic data [17]. C) Regional seismic profile across the western part of the paleo Danube delta in SW to NE direction, depicting the geological setting. The location of this regional seismic profile is marked as line AB in (A). Interpretation of the seismic data according to Zander et al. [2017].

Figure 2: A) Computational domain shown on top of the geological setting (outlined in black). The base of the paleo seafloor at t = 300 ka BP, PSF-C, marks the top boundary of our computational domain. The corresponding base of the GHSZ (green line) was calculated at 400 m sediment depth, thus approximately matching the position of BSR 4. Further added sediment layers, and their deposition times (event1,2,3), and corresponding paleo seafloors (PSF-B, PSF-A, SF-0) are depicted as blue lines. B) pTS conditions in the computational domain at t = 300 ka BP. Temperature distribution follows a regional thermal gradient of 35°C/km with $T = 4^{\circ}$C at PSF-C, and pressure distribution is hydrostatic with $P = 15$ MPa at PSF-C. Salinity is assumed to be constant throughout the domain, and porewater is assumed to be fully saturated with dissolved methane. Initial GH distribution is prescribed according to Eqn.7 and the corresponding $V_{h,0}$ values are given in Table 1 for each scenario.

Figure 3: Comparison of numerical gas saturation profile after a simulation time of 300 ka, i.e. at $t = 0$ ka BP, with the regional seismic profile. A good match was found for parameter values of $V_{h,0} = 10 \ \ m^3/m^2$, $k_d = 10^{-15} \ \ \text{mol}/(m^2 \ \text{Pa} \ s)$, and $k_f = 10^{-13} \ \ \text{mol}/(m^2 \ \text{Pa})$.

Figure 4: GH (a-c) and free gas (d-f) saturations as well as the corresponding GHSZ (i.e., +1: stable GH; -1: unstable GH) (g-i) for the best match scenario (ID 2: $V_{h,0} = 10 \, m^3/m^2$, $k_d = 10^{-15}$ mol$/(m^2$ Pa $s)$, and $k_f = 10^{-13}$ mol$/(m^2$ Pa $s)$) at (a,d,g) the end of the first sediment deposition event at $t = 240$ ka BP, (b,e,h) the end of the second sediment deposition event at $t = 137$ ka BP, and (c,f,i) the end of the third sediment deposition event at $t = 0$ ka BP. Also shown in (g-i) are the gas phase velocities as vectors scaled to their magnitude.

Figure 5: Gas pore-pressure (a-c), temperature (d-f), dissolved methane mole-fraction (g-i), and dissolved salt mole-fraction (j-l) for the best match scenario (ID 2: $V_{h,0} = 10\ m^3/m^2$, $k_d = 10^{-15}$ mol/(m^2 Pa s), and $k_f = 10^{-13}$ mol/(m^2 Pa s)) at (a,d,g,j) the end of the first sediment deposition event at $t = 240$ ka BP, the (b,e,h,k) end of the second sediment deposition event at $t = 137$ ka BP, and (c,f,i,l) the end of the third sediment deposition event at $t = 0$ ka BP.

Figure 6: Free-gas (a,c,e,g,i) and hydrate (b,d,f,h,j) saturation profiles at $t = 137$ ka BP (i.e., at the end of the second sedimentation event) for simulation scenarios with different initial GH volumes: (a,b) $V_{h,0} = 15\ m^3/m^2$ (scenario 1), (c,d) $V_{h,0} = 10\ m^3/m^2$ (scenario 2), (e,f) $V_{h,0} = 6\ m^3/m^2$ (scenario 3), (g,h) $V_{h,0} = 1.8\ m^3/m^2$ (scenario 4), and (i,j) $V_{h,0} = 0.6\ m^3/m^2$ (scenario 5). In all model scenarios, GH dissociation and formation rate constants are $k_d = 10^{-15}$ mol/(m^2 Pa s), and $k_f = 10^{-13}$ mol/(m^2Pa s).

Figure 7: GH saturation at $t = 137$ ka BP for scenarios 2 (best match), 6, 7, 8, and 9. The figure shows the effect of varying GH formation and dissociation rate constants on the distribution of gas hydrate layers.

Figure 8: Free-gas saturation at $t = 137$ ka BP for scenarios 2 (best match), 6, 7, 8, and 9. The figure shows the effect of varying GH formation and dissociation rate constants on the appearance of multiple free gas zones.

Highlights

- This study simulates the sedimentation-driven development of multiple stacked BSRs in the Danube paleo-delta, Black Sea.
- Formation of multiple BSRs in the Black Sea is controlled by the sequence of sedimentation events of the levees induced by sea-level changes.
- Kinetics of phase transitions plays a key role in the coexistence, location, and timing of the multiple BSRs.
- Development of multiple stacked BSRs is possible only under a narrow range of parameters, unique for the Danube delta setting.

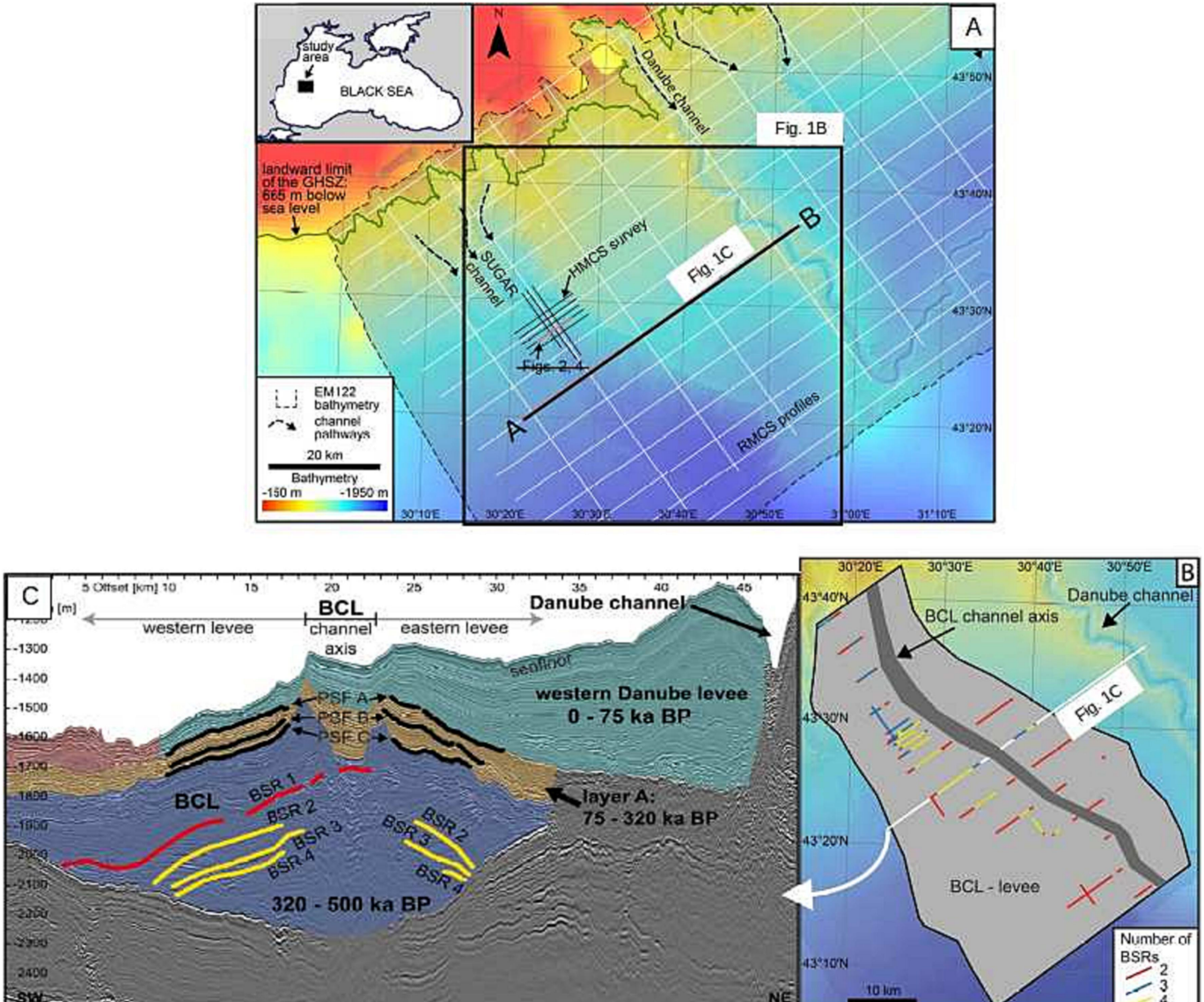
study area
BLACK SEA
N
A
Danube channel
Fig. 1B
landward limit of the GHSZ: 665 m below sea level
SUGAR channel
HMCS survey
Fig. 1C
B
A
Figs. 2, 4
RMCS profiles
EM122 bathymetry
channel pathways
20 km
Bathymetry
-150 m
-1950 m
43°50'N
43°40'N
43°30'N
43°20'N
30°10'E
30°20'E
30°30'E
30°40'E
30°50'E
31°00'E
31°10'E
C
5 Offset [km] 10
15
20
25
30
35
40
45
[m]
western levee
BCL
channel axis
eastern levee
Danube channel
seafloor
western Danube levee
0 - 75 ka BP
PSF A
PSF B
PSF C
BCL
BSR 1
BSR 2
BSR 3
BSR 4
layer A:
75 - 320 ka BP
320 - 500 ka BP
-1300
-1400
-1500
-1600
-1700
-1800
-1900
-2000
-2100
-2200
-2300
-2400
SW
NE
B
30°20'E
30°30'E
30°40'E
30°50'E
43°40'N
43°30'N
43°20'N
43°10'N
Danube channel
BCL channel axis
Fig. 1C
BCL - levee
10 km
Number of BSRs
2
3
4

Figure 1

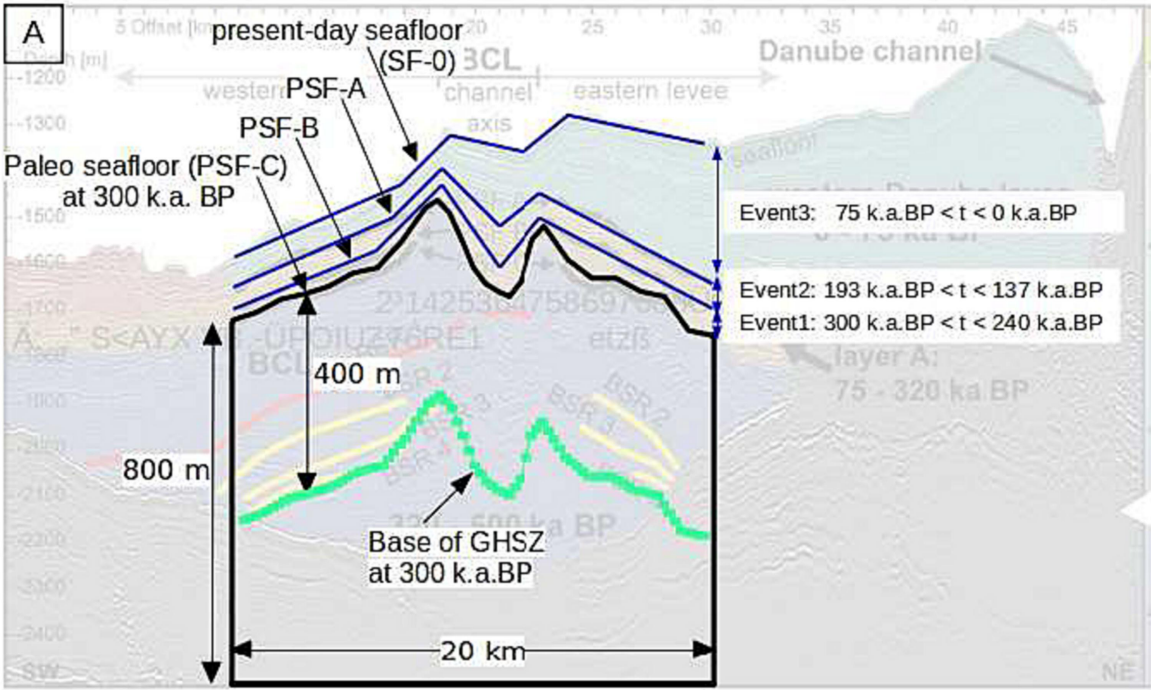
A
present-day seafloor
(SF-0)
PSF-A
PSF-B
Paleo seafloor (PSF-C)
at 300 k.a. BP
Event3: 75 k.a.BP < t < 0 k.a.BP
Event2: 193 k.a.BP < t < 137 k.a.BP
Event1: 300 k.a.BP < t < 240 k.a.BP
400 m
800 m
Base of GHSZ
at 300 k.a.BP
20 km
Danube channel
western
channel
eastern levee
axis
layer A:
75 - 320 ka BP
SW
NE

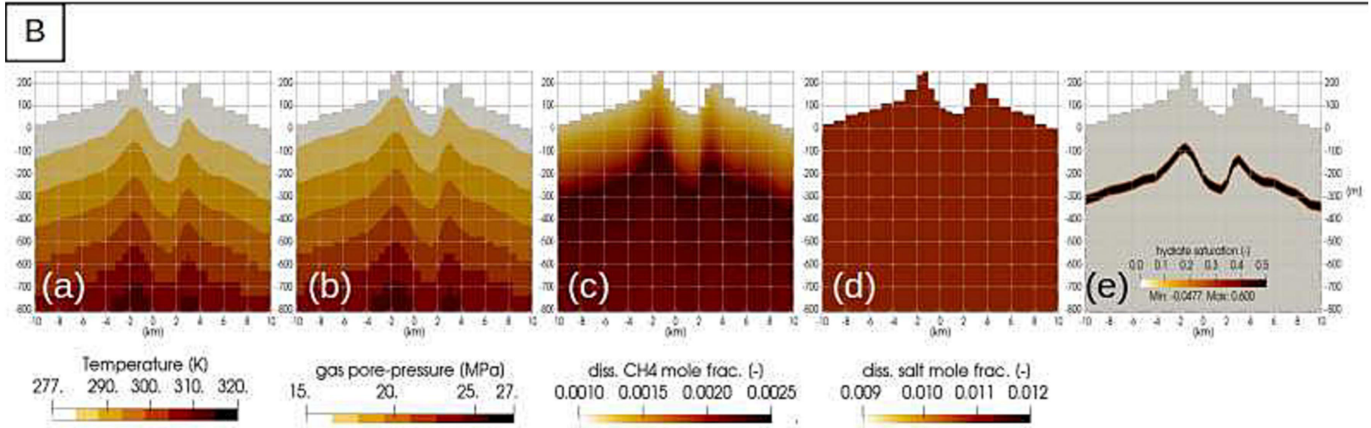
B
(a)
(b)
(c)
(d)
(e)
(km)
hydrate saturation (-)
0.0 0.1 0.2 0.3 0.4 0.5
Min: -0.0477 Max: 0.600
Temperature (K)
277. 290. 300. 310. 320.
gas pore-pressure (MPa)
15. 20. 25. 27.
diss. CH4 mole frac. (-)
0.0010 0.0015 0.0020 0.0025
diss. salt mole frac. (-)
0.009 0.010 0.011 0.012

Figure 2

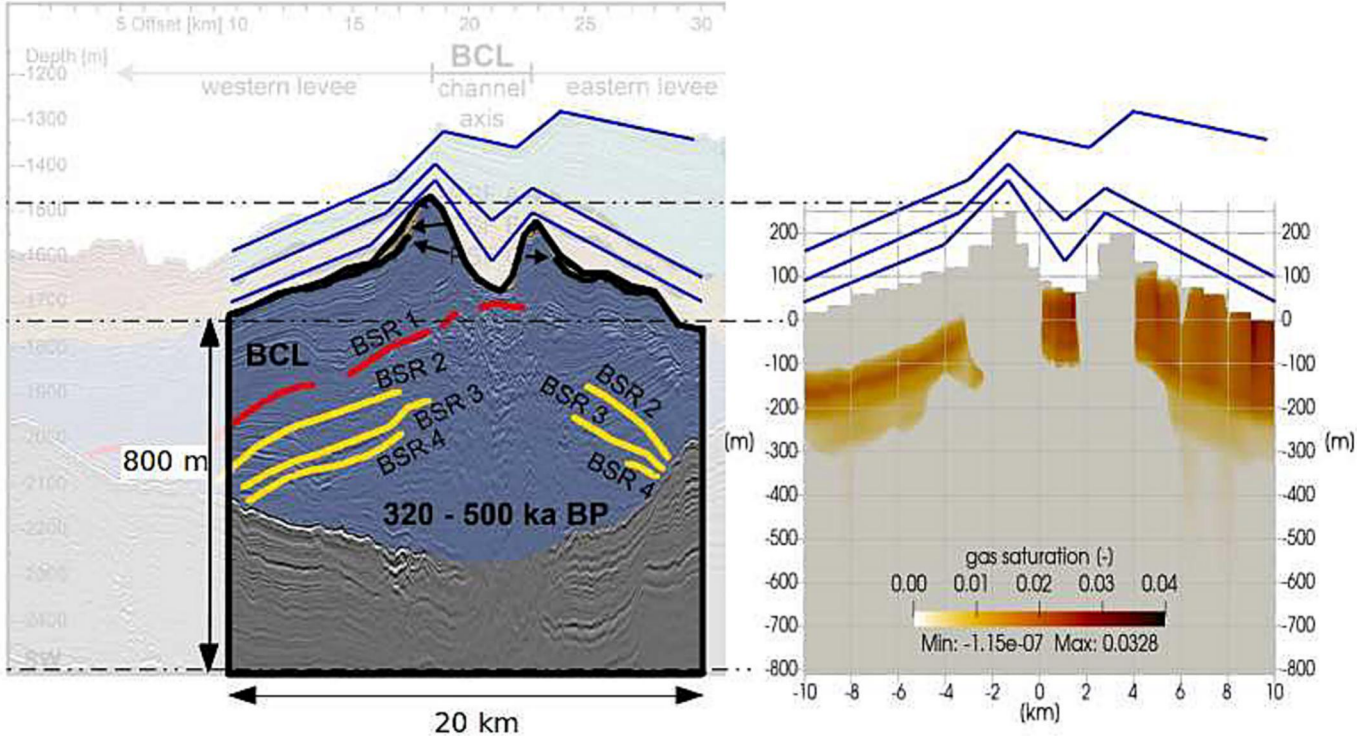
S Offset [km] 10
15
20
25
30
Depth [m]
BCL
western levee
channel axis
eastern levee
BCL
BSR 1
BSR 2
BSR 3
BSR 4
BSR 3
BSR 2
BSR 4
800 m
320 - 500 ka BP
20 km
(m)
gas saturation (-)
0.00 0.01 0.02 0.03 0.04
Min: -1.15e-07 Max: 0.0328
(km)

Figure 3

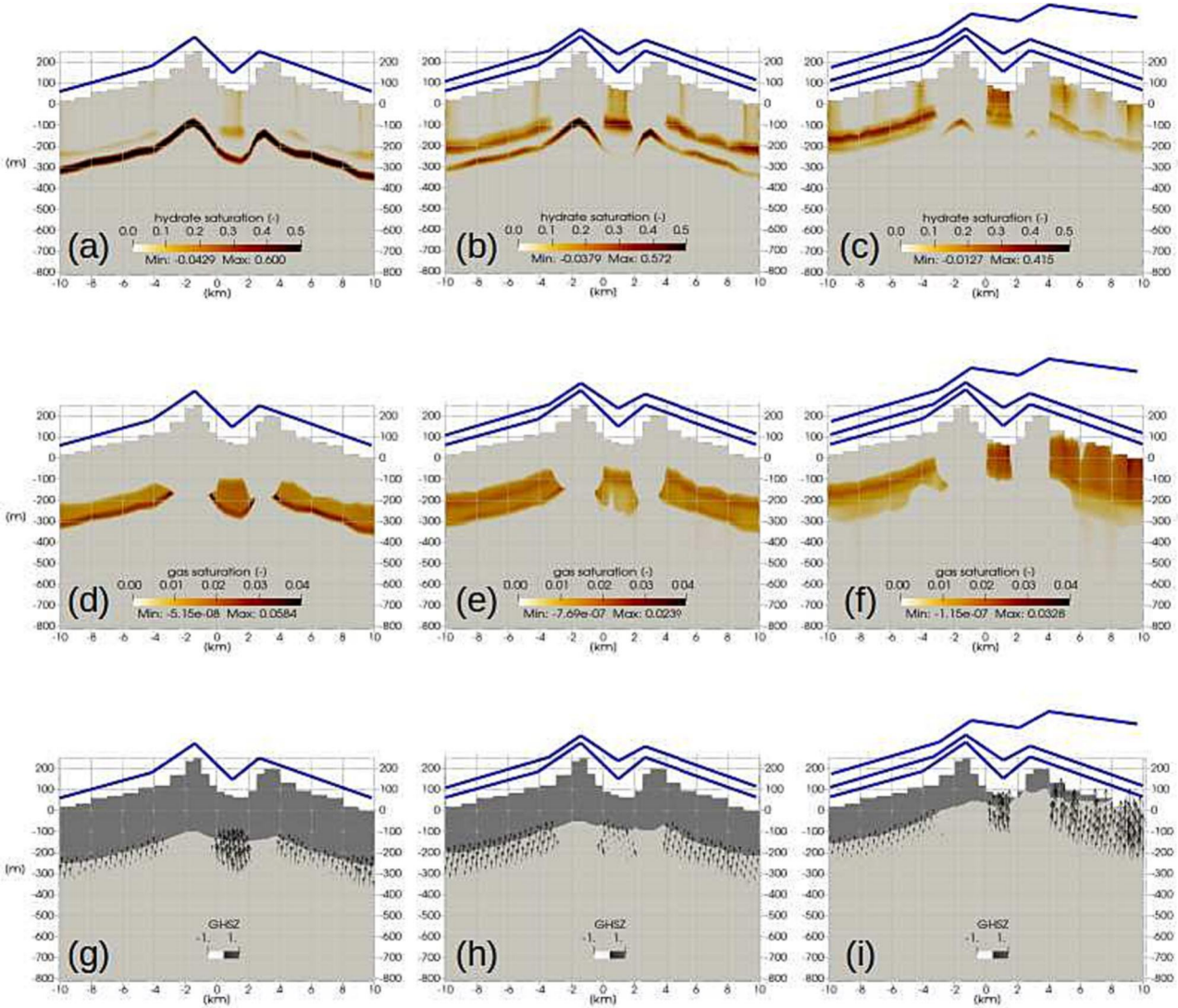
(a)
hydrate saturation (-)
0.0 0.1 0.2 0.3 0.4 0.5
Min: -0.0429 Max: 0.600
(b)
hydrate saturation (-)
0.0 0.1 0.2 0.3 0.4 0.5
Min: -0.0379 Max: 0.572
(c)
hydrate saturation (-)
0.0 0.1 0.2 0.3 0.4 0.5
Min: -0.0127 Max: 0.415
(d)
gas saturation (-)
0.00 0.01 0.02 0.03 0.04
Min: -5.15e-08 Max: 0.0584
(e)
gas saturation (-)
0.00 0.01 0.02 0.03 0.04
Min: -7.69e-07 Max: 0.0239
(f)
gas saturation (-)
0.00 0.01 0.02 0.03 0.04
Min: -1.15e-07 Max: 0.0328
(g)
GHSZ
-1. 1.
(h)
GHSZ
-1. 1.
(i)
GHSZ
-1. 1.
(m)
(km)

Figure 4

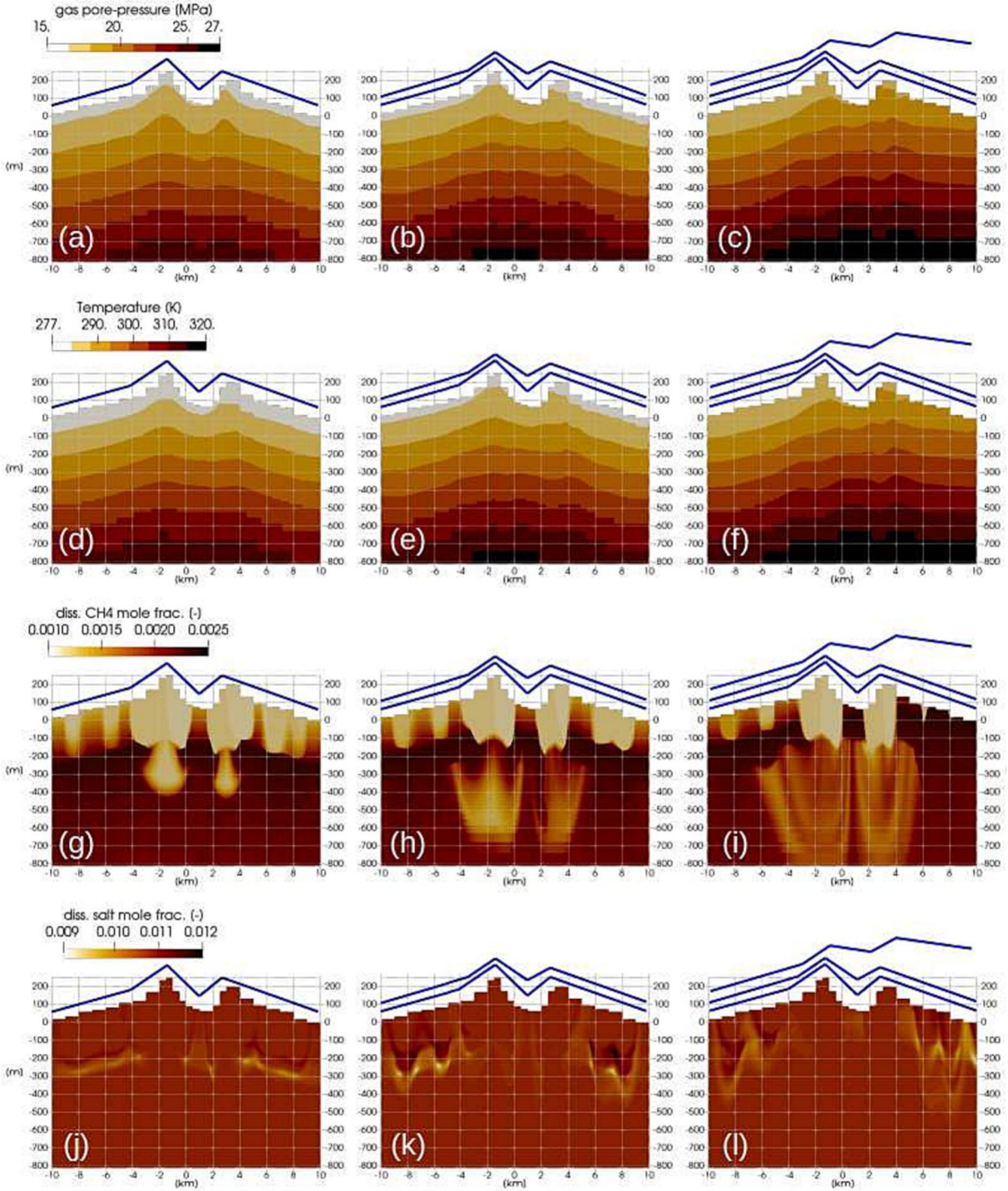
gas pore-pressure (MPa)
15. 20. 25. 27.
Temperature (K)
277. 290. 300. 310. 320.
diss. CH4 mole frac. (-)
0.0010 0.0015 0.0020 0.0025
diss. salt mole frac. (-)
0.009 0.010 0.011 0.012
(m)
(km)
(a)
(b)
(c)
(d)
(e)
(f)
(g)
(h)
(i)
(j)
(k)
(l)

Figure 5

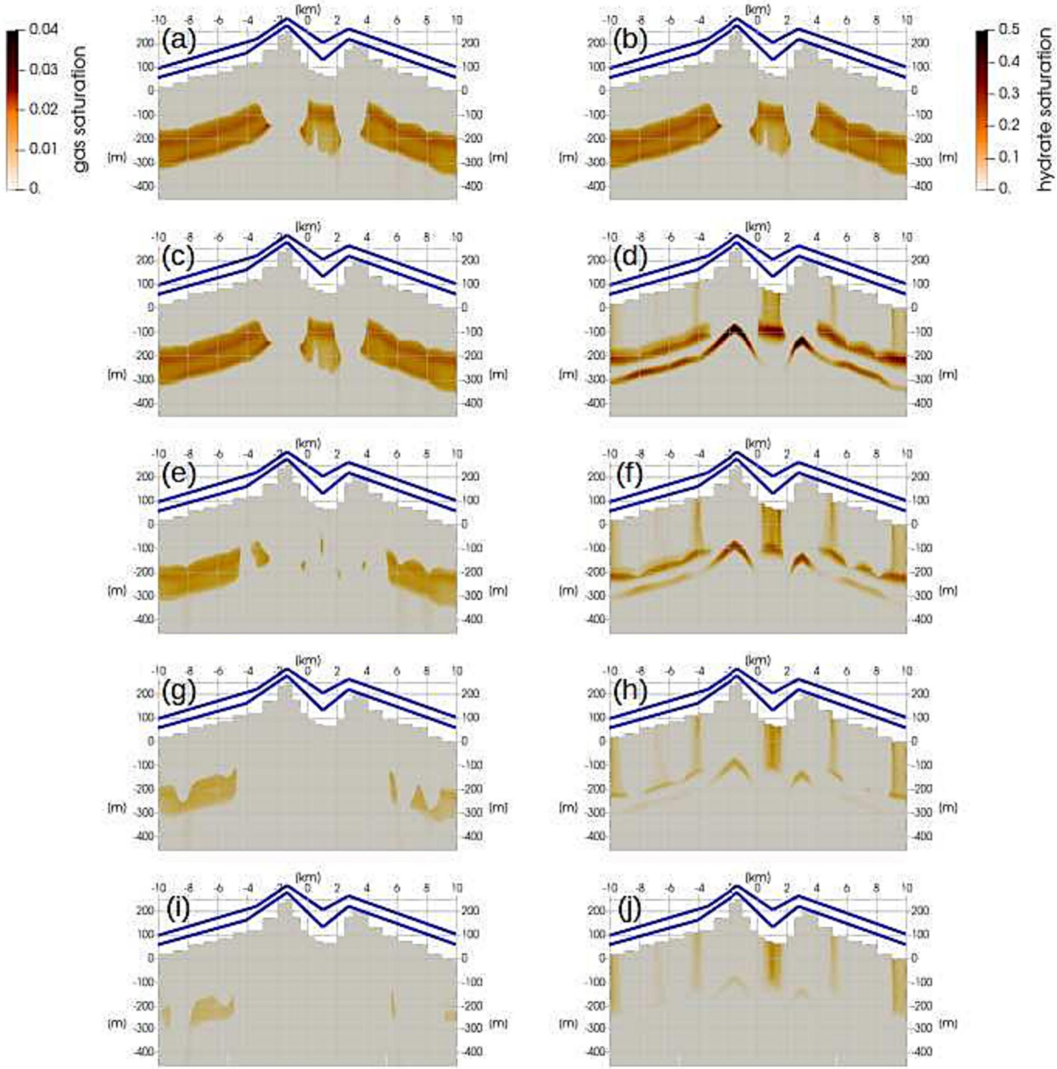
0.04
0.03
0.02
0.01
0.
gas saturation
0.5
0.4
0.3
0.2
0.1
0.
hydrate saturation
(a)
(b)
(c)
(d)
(e)
(f)
(g)
(h)
(i)
(j)
(km)
(m)

Figure 6

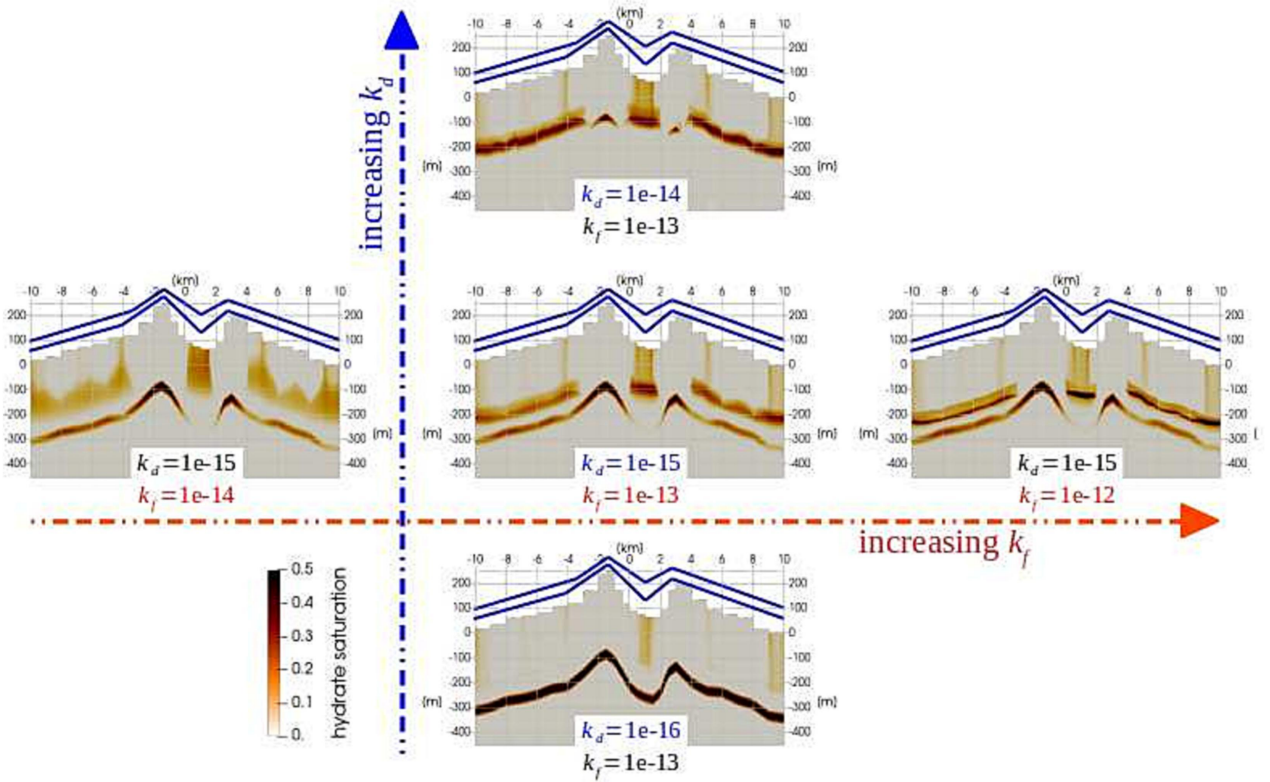
increasing k_d
increasing k_f
k_d=1e-14
k_f=1e-13
k_d=1e-15
k_f=1e-14
k_d=1e-15
k_f=1e-13
k_d=1e-15
k_f=1e-12
k_d=1e-16
k_f=1e-13
hydrate saturation
0.5
0.4
0.3
0.2
0.1
0.
(km)
(m)

Figure 7

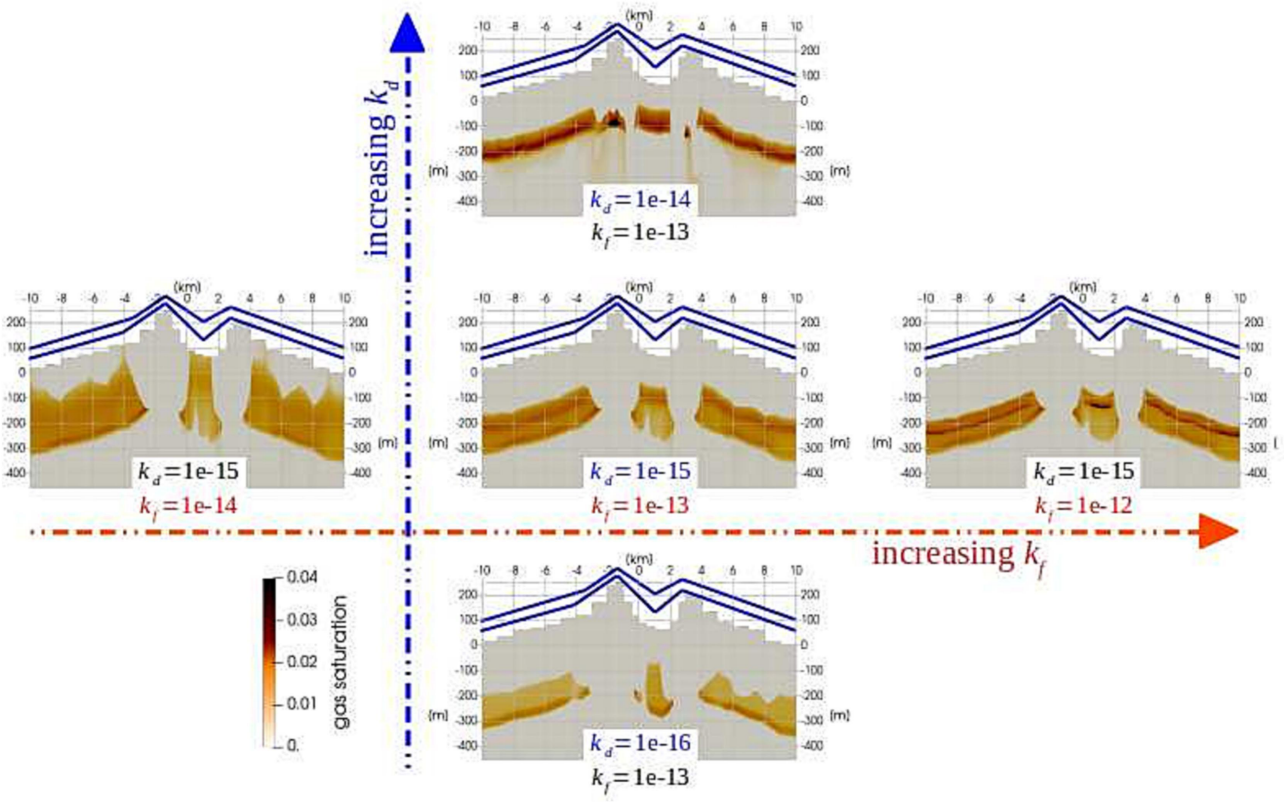
increasing k_d
increasing k_f
k_d=1e-14
k_f=1e-13
k_d=1e-15
k_f=1e-14
k_d=1e-15
k_f=1e-13
k_d=1e-15
k_f=1e-12
k_d=1e-16
k_f=1e-13
gas saturation
0.04
0.03
0.02
0.01
0.
(km)
(m)

Figure 8